



Characterization of video disdrometer uncertainties and impacts on estimates of snowfall rate and radar reflectivity

N. B. Wood¹, T. S. L'Ecuyer², F. L. Bliven³, and G. L. Stephens⁴

¹Cooperative Institute for Meteorological Satellite Studies, University of Wisconsin – Madison, Madison, Wisconsin, USA

²Department of Atmospheric and Oceanic Sciences, University of Wisconsin – Madison, Madison, Wisconsin, USA

³Earth Sciences Division, NASA Goddard Spaceflight Center, Wallops Island, Virginia, USA

⁴Center for Climate Sciences, Jet Propulsion Laboratory, California Institute of Technology, Pasadena, California, USA

Correspondence to: N. B. Wood (norman.wood@ssec.wisc.edu)

Received: 4 March 2013 – Published in Atmos. Meas. Tech. Discuss.: 11 July 2013

Revised: 4 November 2013 – Accepted: 23 November 2013 – Published: 20 December 2013

Abstract. Estimates of snow microphysical properties obtained by analyzing collections of individual particles are often limited to short timescales and coarse time resolution. Retrievals using disdrometer observations coincident with bulk measurements such as radar reflectivity and snowfall amounts may overcome these limitations; however, retrieval techniques using such observations require uncertainty estimates not only for the bulk measurements themselves, but also for the simulated measurements modeled from the disdrometer observations. Disdrometer uncertainties arise due to sampling and analytic errors and to the discrete, potentially truncated form of the reported size distributions. Imaging disdrometers such as the Snowflake Video Imager and 2-D Video Disdrometer provide remarkably detailed representations of snow particles, but view limited projections of their three-dimensional shapes. Particle sizes determined by such instruments underestimate the true dimensions of the particles in a way that depends, in the mean, on particle shape, also contributing to uncertainties. An uncertainty model that accounts for these uncertainties is developed and used to establish their contributions to simulated radar reflectivity and snowfall rate. Viewing geometry effects are characterized by a parameter, ϕ , that relates disdrometer-observed particle size to the true maximum dimension of the particle. Values and uncertainties for ϕ are estimated using idealized ellipsoidal snow particles. The model is applied to observations from seven snow events from the Canadian CloudSat/CALIPSO Validation Project (C3VP), a mid-latitude cold-season cloud and precipitation field experiment. Typical total uncertainties are 4 dB for reflectivity and

40–60 % for snowfall rate, are highly correlated, and are substantial compared to expected uncertainties for radar and precipitation gauge observations. The dominant sources of errors are viewing geometry effects and the discrete, truncated form of the size distributions. While modeled Z_e – S relationships are strongly affected by assumptions about snow particle mass properties, such relationships are only modestly sensitive to ϕ owing to partially compensating effects on both the reflectivity and snowfall rate.

1 Introduction

Estimates of snow particle microphysical properties made with surface observations have typically involved measurements of individual particles (Nakaya and Terada, 1935; Kajikawa, 1972; Mitchell et al., 1990). These methods provide highly detailed descriptions of particles, but the samples have necessarily been small in number and short in duration due to the high amount of effort required. This makes difficult the evaluation of the environmental distributions of the microphysical properties of snowfall and of the temporal evolution of these properties during snowfall events. This information, particularly regarding the environmental distributions, is essential for the development of snowfall retrievals using Bayesian techniques, which generally require a priori information about snow microphysical properties.

Disdrometer-based analyses have the potential to overcome the shortcomings of manual, single-particle observations by providing larger sample sizes and longer-duration

sampling at high time resolution. Specifically, disdrometer observations of particle size distributions (PSDs) in concert with observations of radar reflectivity or accumulated snow mass have been used to estimate snow bulk and microphysical properties. Brandes et al. (2007) used 2-D video disdrometer and snow accumulation observations to estimate snow bulk densities. Huang et al. (2010) also used 2-D video disdrometer observations, along with C-band radar reflectivities, to estimate the parameters of snow particle mass–dimension relations. In analyses such as these, the observed PSDs are used to model radar reflectivity or snowfall accumulation, and the modeled values are then fitted to observed reflectivities or accumulations by adjusting snow microphysical properties.

While uncertainties in the observed reflectivities or accumulations contribute to uncertainties in the estimated microphysical properties, so too do uncertainties in the modeled reflectivities or accumulations. These modeled quantities require integration of terms incorporating the observed PSDs, and the disdrometers introduce particular uncertainties in these observed PSDs. The sources of uncertainty include factors related to the integration itself (upper and lower bounds, and the discrete, numerical treatment of the integral), and uncertainties in the integrands. In this work, the contributions of disdrometer uncertainties to uncertainties in models for near-Rayleigh radar reflectivity and for snowfall rate are evaluated. These uncertainty estimates are essential for use in retrievals that would use coincident ground-based observations of radar reflectivity and snowfall rate or accumulations to estimate snow microphysical properties. The results are also used to estimate the effects of these uncertainties on so-called Ze–S relationships which relate radar reflectivity to snowfall rate. Disdrometer uncertainties are specific to the measurement techniques and sampling strategies used by a particular instrument, and this work focuses on measurements from the Canadian CloudSat/CALIPSO Validation Project (C3VP, Hudak et al., 2006); however, it is anticipated that the methods can be applied to other datasets which employ similar instruments.

Section 2 describes the C3VP disdrometer observations and the measurement methods for these instruments. Section 3 describes models for simulation of snowfall rate and Rayleigh radar reflectivity from the disdrometer observations. Uncertainties for simulated reflectivities and snowfall rates are characterized in Sect. 4; then the results of applying these forward models and uncertainty characterizations to the C3VP observations are given in Sect. 5. Finally, Sect. 5 discusses the implications of these uncertainties for estimation problems using modeled reflectivities and snowfall rates.

2 Snow particle observations

During Northern Hemisphere winter 2006/2007, an extensive set of surface- and aircraft-based in situ and remote

sensing observations of clouds and precipitation was collected in south-central Ontario as part of C3VP (Hudak et al., 2006). An enhanced surface measurement site operated at the Meteorological Service of Canada’s Centre for Atmospheric Research Experiments (CARE) at Egbert, Ontario, approximately 80 km north of Toronto.

A number of instruments installed at CARE provided observations of snow particles, including the NASA Snowflake Video Imager (SVI) (Newman et al., 2009) and Colorado State University’s 2-D Video Disdrometer (2DVD) (Thurai and Bringi, 2005). The SVI uses a video camera to capture 2-D images of particles. In each image frame, the SVI directly observes a 3-D volume defined by the camera’s 2-D field of view and the depth of field (Newman et al., 2009). For a single image frame, the discrete size distribution is

$$N(D_i) = \frac{1}{\Delta D_i} \sum_{j=1}^{j=Np_i} \frac{1}{A_{i,j} L_{i,j}}, \quad (1)$$

where D_i is the characteristic particle size for the i th bin, $A_{i,j}$ is the area of the camera field of view and $L_{i,j}$ is the depth of field associated with the j th particle in the i th size bin. Np_i is the total number of particles in the size bin and ΔD_i is the bin width. Both the field of view and depth of field vary with particle size. Typically, multiple image frames contribute to an observed size distribution, and the total sample volume increases with each frame, giving

$$N(D_i) = \frac{1}{N_f \Delta D_i} \sum_{k=1}^{k=N_f} \sum_{j=1}^{j=(Np_i)_k} \frac{1}{A_{ijk} L_{ijk}}, \quad (2)$$

where N_f is the number of frames and $(Np_i)_k$ is the total number of particles in the k th image frame and the i th bin.

The 2DVD uses two horizontal light sheets, parallel but offset in the vertical, and each light sheet illuminates a horizontal array of photodetectors in a line scan camera. As a particle falls through a light sheet, it shadows some of the photodetectors, and the array is scanned rapidly to determine which photodetectors are shadowed. A stack of horizontal shadow images of the particle results from the scans and, from this stack, information about the dimensions of the particle can be obtained. The light sheets are orthogonal, so particles are observed from two different directions (Hanesch, 1999; Kruger and Krajewski, 2002; Schönhuber et al., 2007).

If a particle is observed by both cameras and the corresponding images can be matched, the time interval between the two images can be used to determine the particle’s fall-speed. The irregular shape of snow particles complicates image matching, since the orthogonal views will see two distinct sides of a particle and the particle’s orientation may change. Hanesch (1999) defined a matching algorithm which applies a number of criteria to match particle images. The criteria are based on the vertical extent of the particles, the ratio of the widths observed by the two cameras, the ratio of maximum width to height, and an allowed range of fallspeeds.

Huang et al. (2010) used similar criteria but applied weights to each criterion, and the best match was chosen based on the image whose weighted sum is a maximum. The 2DVD observations used in this work are the results of the analysis of Huang et al. (2010). The observations report the characteristics of individual particles for which matching succeeded. These characteristics include fallspeed and several measures of particle size, along with the time at which the particle fell through the instrument.

Given particle sizes and fallspeeds, the 2DVD particle size distribution can be determined as

$$N(D_i) = \frac{1}{\Delta t \Delta D_i} \sum_{j=1}^{j=Np_i} \frac{1}{A_{i,j} V_{i,j}}, \quad (3)$$

where i is the index of the size distribution bin, D_i is the characteristic particle size for the i th bin, Δt is the sampling time interval, ΔD_i is the width of the i th size bin, Np_i is the number of particles in the i th size bin, and $A_{i,j}$ and $V_{i,j}$ are respectively the horizontal measurement area and the fallspeed of the j th particle in the i th size bin. Note, however, that if matching does not succeed, the unmatched particle cannot be used in the size distribution calculation since fallspeed is not known and the particle's contribution to the size distribution via Eq. (3) cannot be determined (Hanesch, 1999; Huang et al., 2010). The resulting data loss can lead to errors in the estimated size distribution (Huang et al., 2010).

Because the SVI is not dependent on particle matching, the SVI observations are taken as the primary measure of the snow PSDs for this work. The SVI size distributions are reported in discrete size bins of width 0.25 mm for sizes from 0 to 26 mm at 1 min resolution, but observations of particles smaller than 0.3 mm are discarded during the SVI image processing (Newman et al., 2009). While incomplete matching interferes with accurate determination of a PSD from the 2DVD data, it does not interfere with the measurement of fallspeeds, so the 2DVD observations are used primarily for particle fallspeed data. Also, because of differences in sampling characteristics from the SVI, the 2DVD observations are used to quantify some sources of uncertainty for the SVI.

The observations used in this work are from seven snow events that occurred at CARE during C3VP (Huang et al., 2010). Due to CARE's location southeast of Georgian Bay, it is subject to lake effect snow events. Five of the events occurred during intensive observing periods (IOPs), and are known to be synoptic or lake effect snow storms. While details of the two ex-IOP events are limited, they are expected to also have been lake effect or synoptic. The averaged SVI size distributions for each event (Fig. 1) show that the events represent a range of slopes, indicating the degree of broadening, and particle number concentrations.

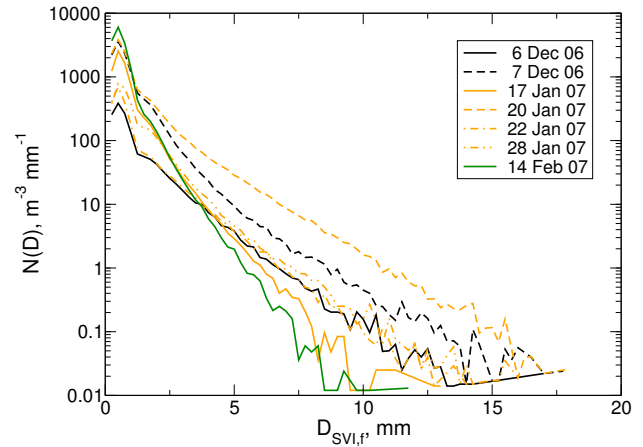


Fig. 1. Averaged SVI size distributions for each C3VP snowfall event.

3 Models for radar reflectivity and snowfall rate

At the wavelengths used by precipitation radars, scattering by most cloud ice and snow particles is near Rayleigh, although scattering by larger, precipitating ice particles may deviate from the Rayleigh approximation (Matrosov et al., 2009). For the uncertainty analyses presented here, particles are assumed to scatter per the Rayleigh approximation for spheres. The errors introduced by this assumption are treated in a forthcoming work. Atlas et al. (1953) showed that low-density, irregularly shaped dry snow particles can be treated as equal volume spheres to calculate radar scattering properties with small error. Provided the radar reflectivity to be simulated is taken to be in close proximity to the radar, attenuation by snow particles and gases under typical winter conditions is negligible (Matrosov, 1998). Given snow particles of sizes D with masses $m(D)$, the effective radar reflectivity factor is then (Battan, 1973)

$$Ze = \frac{36}{\pi^2 \rho_{ice}^2} \frac{\|K_i\|^2}{\|K_w\|^2} \int_{D_{min}}^{D_{max}} N(D) [m(D)]^2 dD, \quad (4)$$

where $N(D)$ is the particle size distribution; $K_w = (n_{liq}^2 - 1)/(n_{liq}^2 + 2)$, n_{liq} is the complex refractive index of liquid water; $K_i = (n_{ice}^2 - 1)/(n_{ice}^2 + 2)$, n_{ice} is the complex refractive index of ice; and the density ρ_{ice} is that of solid ice, 0.917 g cm^{-3} . The particular choice of D , a characteristic dimension of the particles, is not significant provided a consistent choice is used to define both the PSD and the mass–dimension relationship, and the integration limits assert that a finite range of particle sizes contribute to Ze .

Snowfall rate is

$$S = \frac{1}{\rho_{liq}} \int_{D_{min}}^{D_{max}} N(D) m(D) V(D) dD, \quad (5)$$

where $V(D)$ are the particle fallspeeds. In Eq. (5), S is in depth units (e.g., mm h^{-1} of liquid water) and ρ_{liq} is liquid water density. As was true for radar reflectivity, the particular choice of D is not significant, provided a consistent choice is used for defining size distribution, mass and fallspeed.

3.1 Particle dimension

For the mass and fallspeed terms in Eqs. (4) and (5), D is often taken to be the maximum dimension of the particle, D_M , also sometimes referred to as particle diameter. Microphysical parameterizations describing the variation of particle mass and horizontally projected area with particle size are typically expressed in terms of D_M (e.g., Mitchell, 1996). Further, explicit physical models for particle fallspeed depend on a particle dimension which is generally taken to be D_M (Mitchell and Heymsfield, 2005). For irregularly shaped objects like snow particles, however, the various dimensions that can be extracted from the SVI and 2DVD images are different than D_M (Fig. 2), since the disdrometer views a projection of the actual particle (Löffler-Mang and Blahak, 2001). Assuming the observed D is D_M can lead to substantial errors in microphysical parameters determined using coincident radar observations (Appendix).

The expected differences between D_M and the various D were evaluated via simulations using idealized snow particles. Rather than using elliptical silhouettes (Battaglia et al., 2010), the particles were modeled as scalene ellipsoids, and their plane-projected shapes were evaluated. The ellipsoids were defined using three distinct dimensions: a long dimension “ a ” lying nominally in the horizontal plane along the x axis, a short dimension “ b ” also lying nominally in the horizontal plane normal to “ a ” and along the y axis, and a short vertical dimension “ c ” lying along the z axis normal to the x – y plane. The true maximum dimension of the particle is $2a$. Particle orientation was varied by applying uniformly distributed rotations about the z axis and canting at two distinct angles about the x and y axes. The canting angles were distributed over the range of $\pm 21^\circ$ and weighted per a normal distribution with a standard deviation of 9° based on the estimates of Matrosov et al. (2005) for pristine particles.

These various measures of D (Fig. 2) were estimated from the simulated particle images, obtained from the projection of the particle shape onto the x – z plane, averaged over all orientations and compared with D_M for a range of particle aspect ratios defined by b/a and c/a . The value of a was fixed at 0.5, giving a true maximum dimension of 1.0, while $0.05 \leq b \leq a$ and $0.05 \leq c \leq b$. These ranges produce particles that vary from column-like to plate-like to spherical. Values for ϕ , the ratio of D to D_M , range from 0.3 to 1.0 (Fig. 3). $D_{\text{SVI,ec}}$ is sensitive to both the vertical aspect ratio c/a and the horizontal aspect ratio b/a , while $D_{\text{SVI,w}}$ and $D_{\text{SVI,f}}$ are minimally sensitive to the vertical aspect ratio. Of the latter, $D_{\text{SVI,f}}$ shows somewhat less sensitivity to the horizontal aspect ratio than does $D_{\text{SVI,w}}$, while $D_{2\text{DVD,w}}$ shows

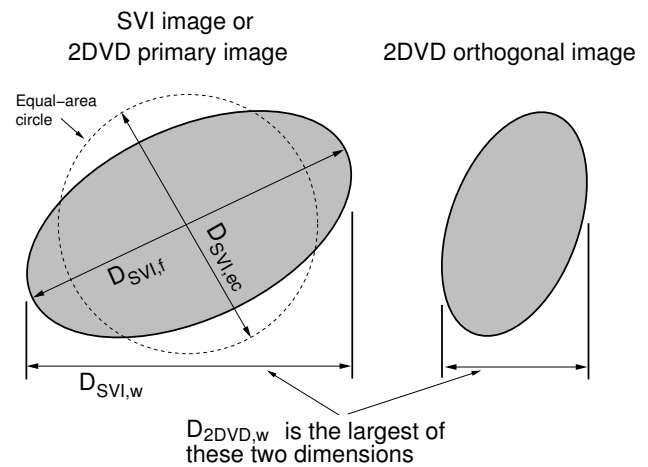


Fig. 2. Particle dimensions as measured by SVI and 2DVD disdrometers: $D_{\text{SVI,ec}}$, diameter of a circle with area equal to that of the SVI particle image; $D_{\text{SVI,w}}$, distance between horizontal extrema of the SVI particle image; $D_{\text{SVI,f}}$, distance between the two furthest removed points on the SVI particle image (feret diameter); and $D_{2\text{DVD,w}}$, maximum of the distance between horizontal extrema obtained from the two 2DVD particle images.

little sensitivity to both vertical and horizontal aspect ratios. For this work, the SVI size distributions were based on $D_{\text{SVI,f}}$ and the 2DVD fallspeeds on $D_{2\text{DVD,w}}$. Taking a typical horizontal aspect ratio of 0.6 (Korolev and Isaac, 2003) gives $\phi_{\text{SVI}} \approx 0.82$ for $D_{\text{SVI,f}}$ with a range of about 0.65 to 1.0. For $D_{2\text{DVD,w}}$, $\phi_{2\text{DVD}} \approx 0.93$ with a range of about 0.88 to 1.0. Calculations using canting angles with a standard deviation of 18° showed similar results, suggesting the variation in ϕ is due mainly to the variation in particle shape rather than canting angle, provided canting angles are not extreme.

Taking the D in Eqs. (4) and (5) to be D_M , the transformation to use the size distributions, fallspeeds and particle sizes based on $D_{\text{SVI,f}}$ and $D_{2\text{DVD,w}}$ proceeds by assuming that ϕ_{SVI} and $\phi_{2\text{DVD}}$ apply to the entire particle range. Transforming the SVI size distributions is done by noting that

$$N(D_M) = N(D_{\text{SVI,f}}) \frac{dD_{\text{SVI,f}}}{dD_M} \quad (6)$$

and, since $D_{\text{SVI,f}} = \phi_{\text{SVI}} D_M$,

$$\frac{dD_{\text{SVI,f}}}{dD_M} = \phi_{\text{SVI}}. \quad (7)$$

The reflectivity model Eq. (4) becomes

$$Z_e = \frac{36}{\pi^2 \rho_{\text{ice}}^2} \frac{\|K_i\|^2}{\|K_w\|^2} \int_{D_{\text{min}}}^{D_{\text{max}}} N(D_{\text{SVI,f}}) \phi_{\text{SVI}} \left[m \left(\frac{D_{\text{SVI,f}}}{\phi_{\text{SVI}}} \right) \right]^2 \frac{dD_{\text{SVI,f}}}{\phi_{\text{SVI}}}, \quad (8)$$

where the ϕ_{SVI} terms in the numerator and denominator have been retained to show explicitly the transformation to

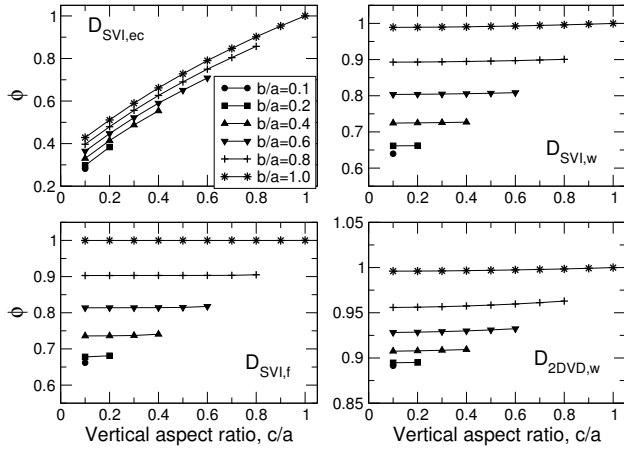


Fig. 3. Values of ϕ , the ratio of D observed by SVI and 2DVD disdrometers to true maximum dimension D_M .

D_M . The snowfall rate model Eq. (5) becomes

$$S = \frac{1}{\rho_{\text{liq}}} \int_{D_{\text{min}}}^{D_{\text{max}}} N(D_{\text{SVI},f}) \phi_{\text{SVI}} m\left(\frac{D_{\text{SVI},f}}{\phi_{\text{SVI}}}\right) V\left(\frac{D_{2\text{DVD},w}}{\phi_{2\text{DVD}}}\right) \frac{dD_{\text{SVI},f}}{\phi_{\text{SVI}}}. \quad (9)$$

Together, Eqs. (8) and (9) constitute the vector-valued forward model F .

In practice, the predefined discrete SVI size bins based on $D_{\text{SVI},f}$ are converted to discrete bins based on D_M as

$$D_{M,i} = \frac{D_{\text{SVI},f,i}}{\phi_{\text{SVI}}}, \quad (10)$$

where i is the SVI bin index and the discrete SVI size distribution values are transformed as

$$N(D_{M,i}) = N(D_{\text{SVI},f,i}) \phi_{\text{SVI}}. \quad (11)$$

The particle sizes for the 2DVD single-particle fallspeed observations are transformed as

$$D_{M,j} = \frac{D_{2\text{DVD},w,j}}{\phi_{2\text{DVD}}} \quad (12)$$

for the j th particle observed during the SVI measurement interval, after which the fallspeeds can be binned onto the $D_{M,i}$ grid for further processing to obtain expected values $V_{M,i}$ and variances $s^2(V_{M,i})$. The subscript M indicates values evaluated as functions of particle maximum dimension. Terms such as $s^2(\cdot)$ and $s(\cdot, \cdot)$ are used herein to represent variances and covariances, respectively.

4 Sources of uncertainty for modeled reflectivity and snowfall rate

The relationship between the observations simulated by a forward model F and the actual observations y can be written as

$$y = F(x, \tilde{b}) + \epsilon, \quad (13)$$

where x is the observed state and ϵ represents the total error. The forward model has been written to show explicitly the dependence on other parameters, \tilde{b} , where the tilde indicates that these parameters may be known imperfectly. The total error ϵ can be expanded as (Rodgers, 2000)

$$\epsilon = \epsilon_Y + \Delta F(x, b) + \frac{\partial F}{\partial b}(b - \tilde{b}), \quad (14)$$

where ϵ_Y is the contribution from measurement error, the second term on the right is the contribution due to the model's approximate formulation of the actual physical relationship, and the third term on the right is the contribution due to errors in the forward model parameters. These errors may consist of both systematic biases and random components. Once recognized biases have been corrected, the residual uncertainties are characterized by the covariance matrix S_ϵ :

$$\begin{aligned} S_\epsilon &= S_y + S_F + S_B \\ &= S_y + S_F + \mathbf{K}_b \mathbf{S}_b \mathbf{K}_b^T, \end{aligned} \quad (15)$$

where the definitions of the terms on the right parallel those for ϵ . In the third term, which is the contribution due to uncertainty in the model parameters, \mathbf{K}_b is the Jacobian of the model with respect to the parameters and \mathbf{S}_b is the covariance matrix for the parameters. The product $\mathbf{K}_b \mathbf{S}_b \mathbf{K}_b^T$ is denoted as S_B . Uncertainties in the modeled Ze and S are contained in S_F and S_B . Because Ze and S may range over several orders of magnitude, their values and uncertainties were characterized in terms of dBZe and $\log S$, where \log is the common logarithm.

4.1 Uncertainties due to parameters, S_B

The parameters used by the models Eqs. (8) and (9) include the binned, discrete values of $D_{\text{SVI},f,i}$, $N(D_{\text{SVI},f,i})$, and $V_{M,i}$, along with ϕ_{SVI} , $\phi_{2\text{DVD}}$, the dielectric parameters $\|K_i\|^2$ and $\|K_w\|^2$, and the densities ρ_{ice} and ρ_{liq} . Since the models use solid ice and liquid water densities and dielectric parameters, these are not expected to be significant sources of uncertainty and are neglected. In particular, the value of $\|K_i\|^2$ is determined largely by the real part of n_{ice} . Uncertainties in n_{ice} at X-band appear small (Warren and Brandt, 2008, and references therein), and temperature sensitivities appear weak (Mätzler, 2006). Since $\phi_{2\text{DVD}}$ shows little uncertainty compared to ϕ_{SVI} , its uncertainty is neglected as well. While the particle mass–dimension relationship $m(D)$ is likely a significant source of uncertainty, this work focuses on other error sources. The objective here is to characterize the necessary forward model uncertainties for use in a future retrieval which would estimate mass–dimensions relationships and their uncertainties. The remaining sources of uncertainty in S_B are due to uncertainties in the disdrometer observations and are evaluated here.

S_B is in the form of a 2×2 error covariance matrix for reflectivity in dBZe and $\log S$. The covariances

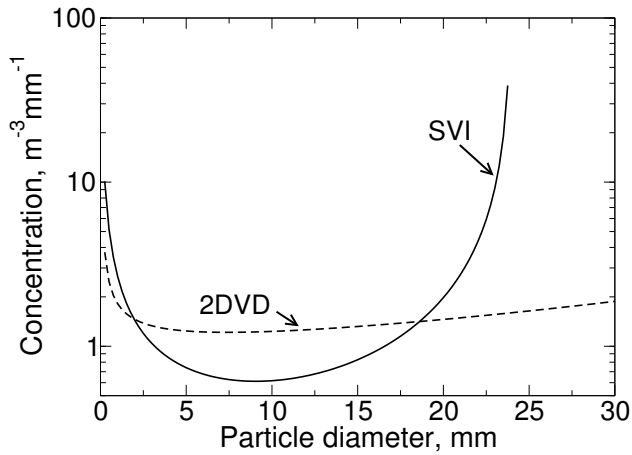


Fig. 4. Comparison of minimum detectable concentrations for the SVI and the 2DVD, assuming 5 min samples, 0.25 mm size bins and spherical particles which must be fully within the sensing area.

4.2.1 Radar reflectivity

Given an assumed mass–dimension relationship based on D_M , the reference radar reflectivity can be calculated directly from a particular sample of 2DVD individual particle observations by summing the backscatter cross sections per unit volume:

$$Z_e = \frac{36}{\pi^2 \rho_{ice}^2} \frac{\|K_i\|^2}{\|K_w\|^2} \frac{1}{\Delta t} \sum_{j=0}^{j=Np} \frac{\left(m \left(\frac{D_{2DVD,w,j}}{\phi_{2DVD}} \right) \right)^2}{A_j V_j}. \quad (18)$$

Corresponding reflectivities can then be calculated from the simulated SVI discrete and discrete-truncated size distributions using Eq. (8) evaluated using the trapezoidal method. The differences between these two reflectivities and the reference reflectivity represent the model errors due to discretization and due to combined discretization and truncation of the size distribution.

A common assumption (e.g., Mitchell, 1996) is that the mass–dimension relationship follows a power law of the form

$$m(D_M) = \alpha D_M^\beta. \quad (19)$$

Provided the mass–dimension relationship Eq. (19) is applicable over the entire size distribution, differences in dBZe will depend on β and not on α , since dBZe differences represent ratios of Ze. Particle mass is usually capped to be no more than that of an ice sphere. This cap means that some dependence on α may occur but is likely to be weak because the cap affects only very small particles.

2DVD observations from the seven C3VP snow events were used to evaluate these errors for a range of values for α and β . Values for α (cgs units) ranged from 0.001 to 0.009 in 0.002 increments, while those for β ranged independently from 1.4 to 2.4 in 0.2 increments. ϕ_{2DVD} was set

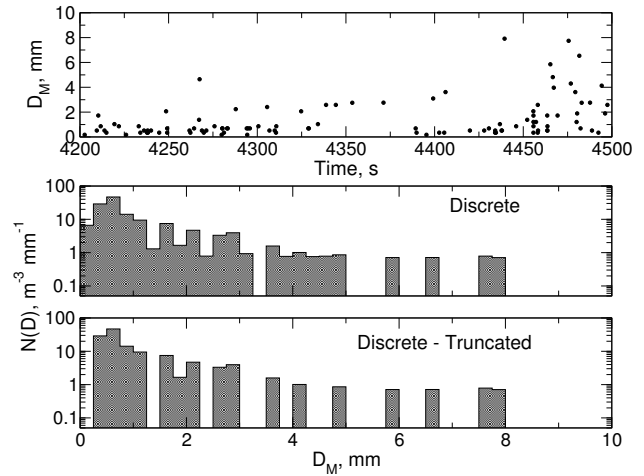


Fig. 5. Example of the processing of 2DVD size observations to form discrete and discrete-truncated particle size distributions: top, observed particle sizes over a 5 min sample; middle, transformation to a discrete PSD based on SVI size bins; and bottom, application of SVI detection limits to mask those bins undetected by the SVI.

to 1.0 for this analysis. To avoid biasing the results to favor frequently occurring samples with trace snow rates, the samples were filtered to exclude those containing fewer than 100 particles. Of the 1273 original samples, this filtering removed 383, 94 % of which had snowfall rates of less than 0.01 mm h^{-1} of liquid water when evaluated using $\alpha = 0.003$ and $\beta = 2.0$. The statistical properties were largely independent of α , as was expected (Table 1). The table shows errors both for discretization with truncation and for discretization only for comparison. Except as noted, this description focuses on the errors due to discretization plus truncation. The reflectivity bias became more negative as β increased, ranging from -0.85 to -1.32 dB, while the residual errors increased from 0.74 to 2.24 dB.

4.2.2 Snowfall rate

The snowfall rate biases and covariances were evaluated following a similar procedure. The reference snowfall rates were calculated directly from the 2DVD individual particle observations as

$$S = \frac{1}{\Delta t \rho_{liq}} \sum_{j=0}^{j=Np} \frac{m \left(\frac{D_{2DVD,w,j}}{\phi_{2DVD}} \right)}{A_j}. \quad (20)$$

Snowfall rates were then calculated with the discrete and discrete-truncated size distributions using Eq. (9) again evaluated via trapezoidal integration with $\phi_{2DVD} = 1.0$. These differences between these rates and the reference rates should scale linearly with α , again except for small departures due to the cap on particle mass, and when evaluated in terms of $\log S$ should have limited dependence on α .

Table 1. Biases, standard deviations of errors and error correlations due to size distribution truncation and discretization for radar reflectivity and snowfall rate. Numbers outside parentheses are due to both discretization and truncation, while those inside parentheses are for discretization only.

β	Reflectivity, dBZe		Snowfall rate, log S		Correlation coefficient
	Bias	SD	Bias	SD	
1.4	-0.85 (-0.72)	0.74 (0.46)	0.016 (0.018)	0.062 (0.060)	0.49 (0.47)
1.6	-0.90 (-0.71)	0.94 (0.46)	0.013 (0.016)	0.062 (0.060)	0.46 (0.39)
1.8	-0.98 (-0.73)	1.22 (0.50)	0.007 (0.010)	0.067 (0.064)	0.48 (0.35)
2.0	-1.08 (-0.74)	1.53 (0.53)	-0.001 (0.003)	0.073 (0.070)	0.51 (0.32)
2.2	-1.19 (-0.76)	1.87 (0.56)	-0.009 (-0.004)	0.081 (0.077)	0.54 (0.29)
2.4	-1.32 (-0.77)	2.24 (0.59)	-0.017 (-0.011)	0.090 (0.085)	0.56 (0.26)

Bias decreased from 0.016 to -0.017 with increasing β , while the residual errors ranged from 0.062 to 0.090 (Table 1). Correlations between the reflectivity and snowfall rate errors are 0.49 to 0.56. The snowfall rate errors proved to be exceptionally sensitive to how $V_{M,i}$ was evaluated. Using a simple mean from a 2DVD sample centered on $D_{M,i}$ and taken over a 0.25 mm size interval resulted in significant positive biases (not shown), likely due to the effects of extreme positive outliers which become increasingly common at smaller particle sizes. To ameliorate these effects, the filter of Brandes et al. (2008) described earlier was applied.

5 Results

The model described above was used to evaluate the contributions of each of the error sources to the total uncertainties in modeled reflectivity and snowfall rate. The model was applied to 1053 independent 5 min SVI samples from the C3VP snow events. Samples were required to contain at least 100 particles. Additionally, since the uncertainty model requires an estimate of the size distribution slope, each sample was required to have at least three non-zero size distribution bins. The modeled uncertainties are sensitive to the parameters of the mass–dimension relationship, and two such relationships were applied: the first from Heymsfield et al. (2010, HE10) with $\alpha = 7.00 \times 10^{-3}$ and $\beta = 2.2$, and the second the frequently used Brown and Francis (1995, BF95) relationship with $\alpha = 2.94 \times 10^{-3}$ and $\beta = 1.9$. Starting from the discretization and truncation errors given by S_F (case A in Table 2), additional sources of uncertainty were introduced incrementally. Case B adds disdrometer analytic and sampling uncertainties, case C adds uncertainties in ϕ for an SVI-like instrument, case D adds uncertainties in ϕ for an instrument using an equal-area D , and case E adds 2DVD fallspeed uncertainties to case C. For all cases, $\phi = 0.82$.

The dominant sources of uncertainty for both dBZe and log S were discretization and truncation, and ϕ . The disdrometer analytic and sampling uncertainties contributed weakly to the total uncertainties, as did the uncertainties in the bin-mean fallspeeds observed by the 2DVD. Uncertainties were

larger for the HE10 mass–dimension relationship than for the BF95 relationship, owing mainly to the larger discretization and truncation errors associated with the larger β value for HE10. For these results, biases and residual errors were calculated for all SVI samples combined. Refinements, such as evaluating bias and residual errors as functions of the modeled reflectivities or snowfall rates, can help reduce residual errors. Evaluating S_F for HE10 microphysics by binning modeled reflectivities and snowfall rates into bins of 2 dBZe and 0.1 in log S , then evaluating bias bin by bin, reduced residual errors for reflectivity from 1.87 to 1.04 dB and for snowfall rate from 0.081 to 0.053 in log S .

When fully accounted, these forward model uncertainties are substantial compared to reasonable estimates of measurement uncertainties. Although these uncertainty estimates do not require assumptions about the shape of their distributions, comparisons can be illustrated by assuming a particular shape. Figure 6 shows sampled probability density functions (PDFs) and uncertainty ellipses calculated for bivariate normal distributions using the uncertainties in Table 2. Considering discretization and truncation errors (Fig. 6a) combined with uncertainties in the representation of particle dimension by the disdrometer (Fig. 6b) gives an uncertainty ellipse similar in size to that for estimated observational errors (Fig. 6c). The observational errors for reflectivity have been represented with standard deviations of 1.5 dB, similar to uncertainties for a well-calibrated operational C-band radar (Thurai et al., 2008). Those for snowfall rate have been estimated at 0.3 in log S , which gives a factor of 2 uncertainty in S . Uncertainties for snowfall measurements on short timescales by automated all-weather gauges (e.g., appropriately fenced OTT Pluvio or Geonor T-200 instruments) are not well characterized, so this value is taken as an approximate upper limit. Although errors in measurements of reflectivity and snowfall rate are independent, the shared dependence of the forward-modeled values on the observed size distributions introduces correlations in the errors in modeled reflectivities and snowfall rates, illustrated by the sloped major axes of the ellipses in panels a and b. Summing the covariance matrices for measurement and model errors per Eq. (15)

Table 2. Contributions to uncertainties in forward-modeled dBZe and log *S*, averaged over 1053 5 min samples. Values of S_F for $\beta = 1.9$ (BF95) were interpolated from Table 1.

Case	Description	HE10			BF95		
		<i>s</i> (dBZe)	<i>s</i> (log <i>S</i>)	<i>s</i> (dBZe, log <i>S</i>)	<i>s</i> (dBZe)	<i>s</i> (log <i>S</i>)	<i>s</i> (dBZe, log <i>S</i>)
A	S_F only	1.87	0.081	0.082	1.38	0.070	0.048
B	A + $s(D_i)$, $s(N(D_i))$	2.01	0.089	0.094	1.50	0.077	0.057
C	B + ($s(\phi) = 0.15$)	4.02	0.196	0.70	3.36	0.187	0.57
D	B + ($s(\phi) = 0.25$)	6.14	0.34	2.00	5.23	0.29	1.48
E	C + $s(V_{M,i})$	4.02	0.22	0.78	3.36	0.197	0.57

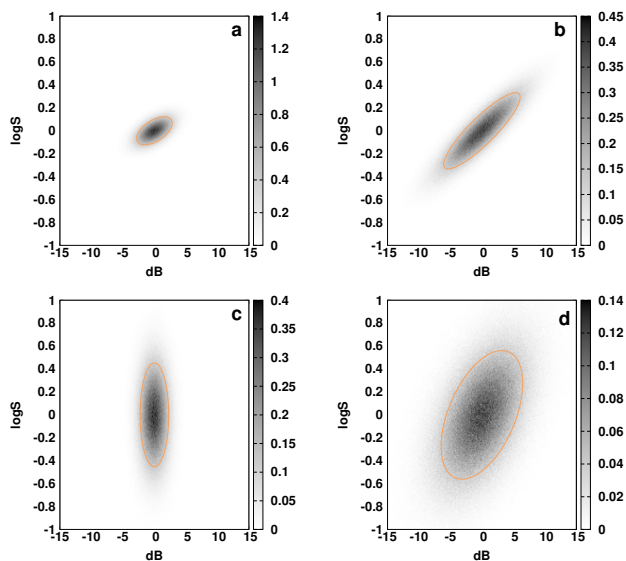


Fig. 6. Uncertainty models for (a) case A alone, (b) case E alone, (c) estimated observational uncertainties, and (d) case E with estimated observational uncertainties. Orange contours show the estimated bounds for 1 standard deviation, while the grayscale illustrates sampled PDFs.

leads to an uncertainty ellipse that is substantially larger than that for either the measurement or model uncertainties alone and which maintains significant error correlations (Fig. 6d). This enlargement of the uncertainty ellipse results from the comparatively large uncertainties in observed versus modeled snowfall rates and in modeled versus observed reflectivities.

5.1 Ze–S relationships

Snowfall rate may be estimated from observed radar reflectivities using so-called Ze–S relationships, typically reported in the form $Z_e = AS^B$. Such relationships can be developed using reflectivities and snowfall rates modeled from observed snow PSDs, although parameterized forms of the PSDs have been used (e.g., Matrosov et al., 2009). These relationships have uncertainties arising from the assumptions about the

particle masses, fallspeeds and scattering properties, as well as from the uncertainties in the observed PSDs. Ze–S relationships were developed for reflectivities, snowfall rates and their uncertainties modeled from the 1053 data points using case E with the HE10 and BF95 mass–dimension relationships. Fits were then performed for modifications to case E in which ϕ was varied to simulate the use of several different unadjusted disdrometer measurements of particle size: E1, a disdrometer using equal-area D_{ec} ; E2, a disdrometer using $D_{SVI,f}$; and E3, a disdrometer using $D_{2DVD,w}$. Fits were performed on the dBZe and log *S* values using the bivariate least-squares estimation method of York et al. (2004), which treats uncertainties in both variables as well as error covariances between the variables, using a function of the form

$$\log S = a + b(\text{dBZe}). \tag{21}$$

The parameters of the fitted relationships show only small sensitivity to differences in the actual observed particle size, represented by changes in ϕ (Table 3, cases E, E1, E2, and E3), but more substantial sensitivity to differences in the mass–dimension relationship (case E, HE10 versus BF95). At 15 dBZe, the differences in ϕ lead to differences in *S* of about $\pm 1.5\%$, while at 30 dBZe the differences in *S* are about $\pm 5\%$. In comparison, changes in the assumed mass–dimension relationship lead to differences in *S* of $\pm 13\%$ at 15 dBZe and $\pm 20\%$ at 30 dBZe. The exponents *B* found here are consistent with values from a number of prior studies, as summarized by Fujiyoshi et al. (1990), and with the results of Huang et al. (2010), who analyzed 2DVD and collocated C-band radar observations for these same snow events and found values ranging from 1.1 to 1.9. For the coefficients *A*, Huang et al. found values in the range of 100 to 300, somewhat smaller than those obtained here, while the studies summarized by Fujiyoshi et al. gave larger values ranging predominantly between 200 and 3000. Huang et al. note that in some cases the large coefficients in these earlier studies may be due to the use of the reflectivity factor, rather than the equivalent reflectivity factor, to develop the Z–S relationships from particle size distributions, which would cause about a factor of 4 increase in *A* (Smith, 1984).

Table 3. Fit results for Ze – S relationships, showing the parameters a and b from Eq. (21). Also shown are parameters A and B used in the more typical form $Ze = AS^B$. Uncertainties (square roots of estimated variances) are given in parentheses.

Case	$m(D)$	D	ϕ	a	b	$s(a, b)$	$Ze = AS^B$		χ^2
							A	B	
E	HE10	D_M	0.82 (0.15)	−1.557 (0.006)	$0.0615 (3 \times 10^{-4})$	-1.39×10^{-6}	339.	1.63	2.67
E	BF95	D_M	0.82 (0.15)	−1.499 (0.005)	$0.0655 (3 \times 10^{-4})$	-1.13×10^{-6}	194.	1.53	2.82
E1	HE10	D_{ec}	1.17 (0.15)	−1.488 (0.004)	$0.0577 (3 \times 10^{-4})$	-7.1×10^{-7}	378.	1.73	2.46
E2	HE10	$D_{SVI,f}$	1.00 (0.15)	−1.508 (0.005)	$0.0591 (3 \times 10^{-4})$	-9.5×10^{-7}	358.	1.69	2.55
E3	HE10	$D_{2DVD,w}$	0.88 (0.15)	−1.540 (0.006)	$0.0606 (3 \times 10^{-4})$	-1.22×10^{-6}	347.	1.65	2.64

6 Conclusions

Typical retrieval and estimation techniques involve minimizing differences between observed and modeled quantities. For these sorts of problems, quantifying the uncertainty characteristics of the model–measurement differences is essential. As an example, in Bayesian optimal estimation the model–measurement difference uncertainties, along with the a priori estimate of the PDF of the retrieved state, determine the posterior distribution of the retrieved state. In general, larger uncertainties in the model–measurement differences will contribute to larger uncertainties in the posterior, retrieved state. Retrieval performance can be gauged based on comparisons of the width of the posterior PDF compared to that of the a priori PDF (e.g., Shannon Information Content; Rodgers, 2000), and so accurate assessments of the model–measurement difference uncertainties contribute to accurate assessments of retrieval performance.

In this particular application, forward model uncertainties are substantial compared to estimated measurement uncertainties, so omitting the contribution of forward model uncertainties to the model–measurement difference uncertainties would likely underestimate uncertainties in the retrieved state and of the retrieval information content. Ignoring the forward model uncertainties may in some cases cause retrieval failure, since the model–measurement difference uncertainties impact the value of the cost function being minimized.

For modeled reflectivities and snowfall rates, the dominant sources of uncertainty are discretization and truncation, and the uncertainty in ϕ . Uncertainties in the discrete values of D_i and $N(D_i)$ provided by the disdrometer and uncertainties in the size bin mean fallspeeds contributed minimally to the total uncertainties. Considering discretization and truncation, truncation contributes more strongly to the total uncertainties. Truncation uncertainties can be reduced by increasing the sample volume, which increases the size at which truncation occurs. For an instrument like the SVI, this can be achieved by increasing the number of image frames in a single sample, by increasing the field of view, or by increasing the depth of field. The number of image frames can be increased by either sampling longer or sampling faster, and there are likely several trade-offs with either approach. For

example, longer sampling will decrease the temporal resolution of the dataset, while faster sampling would likely impact camera hardware, data storage and processing requirements, and potentially increase errors caused when particles are counted repeatedly in successive frames. With faster sampling, it becomes more likely that successive frames no longer observe independent samples of the PSD.

Uncertainties in ϕ contribute at least half of the total uncertainties in modeled reflectivities and snowfall rates. The value of ϕ varies with particle shape and the particular dimensional measurement used by the disdrometer (Fig. 2). The use of dimensional measurements such as feret diameter that reduce the sensitivity of ϕ to particle shape is desirable to reduce these uncertainties. Additional coincident disdrometer observations may also help constrain ϕ or reduce its uncertainties. As an example, although the dual viewing geometries of the 2DVD raise particle matching issues, the $D_{2DVD,w}$ particle size metric gives ϕ values with relatively weak sensitivity to particle shape. The SVI is adaptable to other viewing geometries (e.g., viewing from a more nearly vertical orientation rather than horizontally), and such geometries may prove useful for constraining ϕ .

Finally, while changes in the mass–dimension relationship have a pronounced effect on modeled Ze – S relationships, changes in ϕ affect both reflectivity and snowfall rate somewhat proportionately so that Ze – S relationships are minimally affected. As shown in Table 3, changes in ϕ of 0.82 to 1.17 cause changes in the coefficient of Ze – S relationships of only 339 to 378, and changes in the exponent of only 1.63 to 1.73. Thus disdrometers employing different measures of particle size might be expected to produce similar modeled Ze – S relationships.

Appendix A

Disdrometer dimensional errors

How significant are the errors introduced by treating a disdrometer observation of D as the maximum dimension? An exponential size distribution based on the true maximum dimension D_M is

$$N(D_M) = N_{0,M} \exp(-\lambda_M D_M). \quad (A1)$$

Here and in the following, the subscript M indicates quantities determined from measurements of particle maximum dimension. Transforming this distribution to use an observed dimension $D_{obs} = \phi D_M$ as the independent variable gives

$$N(D_{obs}) = N(D_M) \frac{\partial D_M}{\partial D_{obs}} = \frac{N_{0,M}}{\phi} \exp\left(-\frac{\lambda_M}{\phi} D_{obs}\right), \quad (A2)$$

where it has been assumed that ϕ is constant over the entire distribution. The transformation from D_M to D_{obs} results in a distribution with steeper slope and larger intercept. Although the zeroth moments are the same for both distributions, higher-order moments are different and quantities such as reflectivity which depend on higher-order moments will be affected. Reflectivities can be calculated for both cases, one in which the disdrometer truly observes D_M and a second in which D_{obs} is erroneously taken to be D_M . Applying the mass power law Eq. (19) with the distribution Eq. (A2) and calculating reflectivity per Eq. (4) gives

$$Z_{e_{obs}} = \frac{36\alpha^2}{\pi^2 \rho_{ice}^2} \frac{\|K_i\|^2}{\|K_w\|^2} \frac{N_{0,M}}{\phi} \frac{\Gamma(2\beta + 1)}{(\lambda_M/\phi)^{2\beta+1}}, \quad (A3)$$

while that for distribution Eq. (A1) is

$$Z_{e_M} = \frac{36\alpha^2}{\pi^2 \rho_{ice}^2} \frac{\|K_i\|^2}{\|K_w\|^2} N_{0,M} \frac{\Gamma(2\beta + 1)}{\lambda_M^{2\beta+1}}, \quad (A4)$$

where Γ is the gamma function. The ratio of the reflectivities is

$$\frac{Z_{e_{obs}}}{Z_{e_M}} = \frac{N_{0,M}/\phi}{N_{0,M}} \frac{\lambda_M^{2\beta+1}}{(\lambda_M/\phi)^{2\beta+1}} = \phi^{2\beta}. \quad (A5)$$

Taking a typical horizontal aspect ratio of 0.6 (Korolev and Isaac, 2003) gives $\phi \approx 0.82$ for $D_{obs} = D_{SVI,f}$. A common estimate for β is 1.9 (Brown and Francis, 1995), resulting in a reflectivity ratio of 0.47. Thus Z_e modeled using $N(D_{obs})$ will be underestimated by 3.2 dB. In order for a modeled value of $Z_{e_{obs}}$ to match an observed Z_e , the coefficient α would have to be overestimated by almost 50 %.

Appendix B

Disdrometer uncertainty models

B1 Analytic uncertainties for $D_{SVI,f,i}$ and $N(D_{SVI,f,i})$

The SVI size distribution is determined as shown in Eq. (2). Both A_{ijk} and L_{ijk} depend on particle size:

$$A_{ijk} = (X_{fov} - D_{ijk})(Y_{fov} - D_{ijk}), \quad (B1)$$

$$L_{ijk} = f D_{ijk}, \quad (B2)$$

where X_{fov} and Y_{fov} are the maximum width and height of the frame, f is an empirical factor relating particle size to depth of field, and D_{ijk} is the particle size (Newman et al., 2009). The expression Eq. (B1) embodies an “all-in” requirement, in which the particle must be contained totally within the field of view of the image to be counted. Newman et al. derived the relationship Eq. (B2) using the feret diameter, and this is consistent with the observed D used in these SVI data (note that the SVI,f subscript for D has been dropped for clarity). Combining Eqs. (2), (B1) and (B2) then simplifying the indexing, the size distribution can be written as

$$N(D_i) = \frac{1}{N_f \Delta D_i} \sum_{j=1}^{j=Np_{i,tot}} \frac{1}{(X_{fov} - D_{ij})(Y_{fov} - D_{ij}) f D_{ij}}. \quad (B3)$$

$Np_{i,tot}$ is the total number of particles observed in the i th bin accumulated over all image frames. The number of frames N_f and the frame dimensions X_{fov} and Y_{fov} can be determined accurately, and ΔD_i is a specified constant size bin width, leaving $Np_{i,tot}$, f , and D_{ij} as sources of error.

Errors in the measured particle size D_{ij} are caused by blurring and lack of contrast in the image (Newman et al., 2009). These errors affect the estimates of the field of view A_{ijk} and depth of field L_{ijk} , which then propagate as errors in the calculated size distribution via Eq. (B3). Particle sizing errors also cause particles to be misclassified into size intervals. Since undercounting in one interval will be accompanied by overcounting in nearby intervals, the effects on integrated quantities like reflectivity and snowfall rate calculations in the forward model are expected to be minor and are neglected.

Errors in the count of particles $Np_{i,tot}$ can be caused by reappearance of particles and by obscuration. In environments with very low wind speeds, a slowly falling particle may appear in multiple frames, causing it to be counted multiple times. Winds at 2 m a.g.l. were generally in excess of 1.5 ms^{-1} during the seven snow events, and such repeated counting is not expected to be a concern. Under conditions of high particle concentrations, a particle in the background of the sample volume may be obscured by a particle in the foreground. It is not known to what extent obscuration affects the SVI observations. For small particles, for which concentrations may be high, the depth of field per Eq. (B2) is shallow, making obscuration unlikely. For large particles, depth of field is larger but concentrations are typically low, also making obscuration unlikely. Based on these arguments, errors in $Np_{i,tot}$ due to reappearance and obscuration were neglected.

To estimate the analytic uncertainty, we assume that $Np_{i,tot}$ is measured with negligible uncertainty (e.g., overlapping or doubly counted particles are uncommon). The measurements D_{ij} have uncertainties with variances $s^2(D_{ij})$ that are expected to be independent and identically distributed. The parameter f has uncertainty independent of the uncertainties in D_{ij} with variance $s^2(f)$. Representing $N(D_i)$ as N_i to

simplify notation, Eq. (B3) can be rewritten as

$$N_i = \frac{1}{N_f \Delta D_i} \sum_{j=1}^{j=N_{p_i, \text{tot}}} x_j, \quad (\text{B4})$$

where

$$x_j = \frac{1}{(X_{\text{fov}} - D_j)(Y_{\text{fov}} - D_j)f \cdot D_j} \quad (\text{B5})$$

and where the i subscript for terms inside the sum has been omitted for clarity. The variances $s^2(x_j)$ can be estimated by error propagation as

$$s^2(x_j) = \left(\frac{\partial x_j}{\partial D_j} \right)^2 s^2(D_j) + \left(\frac{\partial x_j}{\partial f} \right)^2 s^2(f). \quad (\text{B6})$$

The variance $s^2(N_i)$ can be found as

$$s^2(N_i) = \left[\left(\frac{\partial N_i}{\partial x_1} \right)^2 s^2(x_1) + \left(\frac{\partial N_i}{\partial x_2} \right)^2 s^2(x_2) + \dots + \left(\frac{\partial N_i}{\partial x_{N_{p_i, \text{tot}}}} \right)^2 s^2(x_{N_{p_i, \text{tot}}}) \right]. \quad (\text{B7})$$

Since $\frac{\partial N_i}{\partial x_j} = \frac{1}{N_f \Delta D_i}$,

$$s^2(N_i) = \left[\frac{1}{N_f \Delta D_i} \right]^2 \left[s^2(x_1) + s^2(x_2) + \dots + s^2(x_{N_{p_i, \text{tot}}}) \right]. \quad (\text{B8})$$

Provided the partial derivatives $\frac{\partial x_j}{\partial D_j}$ do not vary significantly over the size range within a bin, the values of $s^2(x_j)$ will also not vary significantly and can be approximated with a single value $s^2(x)$, giving

$$s^2(N_i) \approx \left[\frac{1}{N_f \Delta D_i} \right]^2 N_{p_i} s^2(x). \quad (\text{B9})$$

Since single-particle measurements were not part of the processed SVI data, the derivatives $\frac{\partial x_j}{\partial D_j}$ and the variances $s^2(D_j)$ were estimated at the expected values of D on the size bin interval between D_i and D_{i+1} . For spherical particles, the uncertainty in particle size has been estimated at 18% (Newman et al., 2009), and that estimate was used for this work even though nonspherical snow particles are observed. Note that D_{ij} in this context is the dimension observed by the disdrometer, not an estimate of the particle maximum dimension. Newman et al. (2009) estimated the uncertainty in depth of field at 15% when particle size is known accurately, suggesting that f has an uncertainty of 15%, which was the value used for this work.

B2 Sampling uncertainties for $D_{\text{SVI},i}$ and $N(D_{\text{SVI},i})$

Sampling errors affect both the number of particles counted in the discrete size intervals and the distribution of particle sizes observed in a particular interval. The number of particles $N_{p_i, \text{tot}}$ in a particular size bin observed arriving in the

disdrometer sample volume at a particular instant is typically taken to be a random deviate (Joss and Waldvogel, 1969) and contributes to sampling uncertainty in the calculated size distribution values. For rainfall, the number of particles observed in a given size bin by a volume sampling device like the SVI is often taken to be a Poisson-distributed random variable (Joss and Waldvogel, 1969; Gertzman and Atlas, 1977; Uijlenhoet et al., 2006). The same approach is taken here for snowfall, considering it to behave as a homogeneous Poisson process during the sampling time interval. The number of particles $N_{p_i, \text{tot}}$ appearing in the SVI sampling volume then follows a Poisson distribution.

The observed particles sizes D_{ij} also vary and are distributed according to a probability density function defined by the size distribution (Uijlenhoet et al., 2006). The observed D_{ij} form a sequence of random variables taken to be independent and identically distributed. As a result, the x_j of Eq. (B5) are also independent and identically distributed. Referring to Eq. (B3), since both the particle sizes D_{ij} and the number of particles $N_{p_i, \text{tot}}$ are realizations of random variables, the form of $N(D_i)$ is seen to be that of a random sum of random variables (Feldman and Valdez-Flores, 2010), also known as a randomly stopped sum.

Letting

$$y_i = \sum_{j=1}^{j=N_{p_i, \text{tot}}} x_j \quad (\text{B10})$$

the variance of y_i can be shown to be

$$V[y_i] = V[x_j] E[N_{p_i, \text{tot}}] + [E[x_j]]^2 V[N_{p_i, \text{tot}}], \quad (\text{B11})$$

(Feldman and Valdez-Flores, 2010) by applying the law of total variance, where $V[\]$ indicates variance and $E[\]$ indicates expectation. Since $N_{p_i, \text{tot}}$ is Poisson-distributed, the best estimate of the expectation and variance is the observed count, so that

$$V[y_i] = N_{p_i, \text{tot}} V[x_j] + N_{p_i, \text{tot}} [E[x_j]]^2. \quad (\text{B12})$$

Thus it is necessary to estimate the expectation and variance for x_j . These can be estimated via Taylor series expansion of $x(D)$. Since uncertainty in f does not contribute to sampling uncertainty, the expectation can be estimated as

$$E[x(D)] \approx x(\mu_D) + \frac{x''(\mu_D)}{2} s_D^2, \quad (\text{B13})$$

where μ_D and s_D^2 are the expectation and variance of D , respectively, and the primes indicate derivatives with respect to D . The variance can be estimated as

$$V[x(D)] \approx (x'(\mu_D))^2 s_D^2. \quad (\text{B14})$$

As noted by Uijlenhoet et al. (2006), the particle size distribution can be written as the product of the total number concentration, N_{tot} , and the probability density function

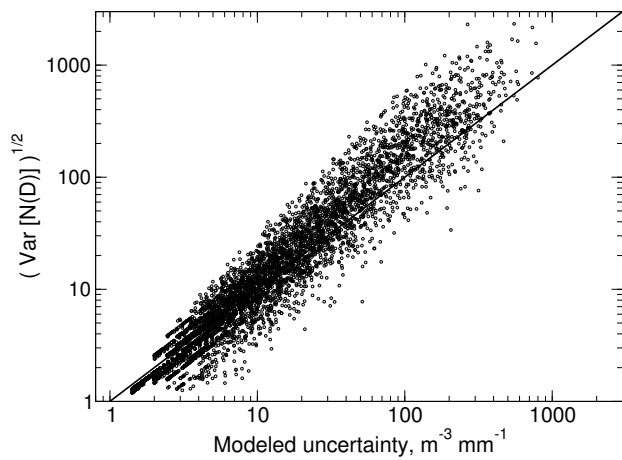


Fig. B1. Comparison of uncertainties estimated from observations (square root of variance computed from samples of 5 1 min particle size distributions) and those calculated from the uncertainty model.

of particle sizes, $p(D)$. Taking the particle sizes to be distributed exponentially gives

$$N(D) = N_{\text{tot}}\lambda \exp(-\lambda D), \quad (\text{B15})$$

from which it can be seen that

$$p(D) = \lambda \exp(-\lambda D). \quad (\text{B16})$$

What is needed are estimates of the expectation and variance of D on subintervals of $p(D)$. For a subinterval bounded by D_i and D_{i+1} , expectation and variance are defined by

$$\mu_D = \frac{\int_{D_i}^{D_{i+1}} p(D)DdD}{\int_{D_i}^{D_{i+1}} p(D)dD} \quad (\text{B17})$$

and

$$s_D^2 = \frac{\int_{D_i}^{D_{i+1}} p(D)(D - \mu_D)^2dD}{\int_{D_i}^{D_{i+1}} p(D)dD}. \quad (\text{B18})$$

Evaluating these integrals for the exponential probability distribution gives

$$\mu_D = D_i + \frac{1}{\lambda} - \frac{(D_{i+1} - D_i)\exp(-\lambda(D_{i+1} - D_i))}{1 - \exp(-\lambda(D_{i+1} - D_i))} \quad (\text{B19})$$

and

$$s_D^2 = \frac{1}{\lambda^2} - \frac{\exp(-\lambda(D_{i+1} - D_i))(D_{i+1} - D_i)^2}{(1 - \exp(-\lambda(D_{i+1} - D_i)))^2}. \quad (\text{B20})$$

The value of λ can be estimated by linear least squares fitting of $\ln(N_i)$ to D_i . Given these last two relationships and λ , the expectation and variance of D can be determined for each size bin. From these, the expectation and variance of

$x(D)$ can be found using Eqs. (B13) and (B14). Next, the variance of y_i can be found via Eq. (B12). Finally, since

$$N_i = \frac{1}{N_f \Delta D_i} y_i, \quad (\text{B21})$$

the variance of N_i is

$$V[N_i] = \left[\frac{1}{N_f \Delta D_i} \right]^2 V[y_i]. \quad (\text{B22})$$

B3 Size distribution uncertainty model evaluation

As a simple check on the validity of the size distribution uncertainty model, distinct samples of the SVI observations were formed by repeatedly collecting five consecutive 1 min SVI size distributions from the observations for one C3VP snow event. Variances were computed bin by bin for each sample. The statistical uncertainty model described above was then applied to the 5 min average size distribution obtained from each sample, and then the modeled analytic and sampling variances for each bin were summed. Both the empirical and modeled uncertainties spanned approximately three orders of magnitude (Fig. B1). At small uncertainties, the modeled and empirical uncertainties were in good agreement. At large uncertainties, the modeled uncertainties for the 5 min size distributions were somewhat smaller than the empirical uncertainties for the 1 min size distributions. Given that the empirical uncertainties apply to 1 min SVI observations, while the modeled uncertainties apply to 5 min averages of the SVI observations, the differences appear reasonable.

Acknowledgements. This work was supported by the National Aeronautics and Space Administration by research grant #NAS5-99327 and by CloudSat subaward #1439268 through the NASA Jet Propulsion Laboratory. Thanks to Gwo-Jong Huang of Colorado State University for making available his 2DVD dataset from C3VP, and to two anonymous reviewers for their constructive comments.

Edited by: G. Baumgarten

References

- Atlas, D., Kerker, M., and Hitschfeld, W.: Scattering and attenuation by non-spherical atmospheric particles, *J. Atmos. Terr. Phys.*, 3, 108–119, 1953.
- Battaglia, A., Rustemeier, E., Tokay, A., Blahak, U., and Simmer, C.: PARSIVEL snow observations: a critical assessment, *J. Atmos. Ocean. Tech.*, 27, 333–344, doi:10.1175/2009JTECHA1332.1, 2010.
- Battan, L. J.: Radar observation of the atmosphere, TechBooks, Herndon, VA, 324 pp., 1973.
- Brandes, E. A., Ikeda, K., Zhang, G., Schoenhuber, M., and Rasmussen, R. M.: A statistical and physical description

- of hydrometeor distributions in Colorado snowstorms using a video disdrometer, *J. Appl. Meteorol. Clim.*, 46, 634–650, doi:10.1175/JAM2489.1, 2007.
- Brandes, E. A., Ikeda, K., and Thompson, G.: Aggregate terminal velocity/temperature relations, *J. Appl. Meteorol. Clim.*, 47, 2729–2736, doi:10.1175/2008JAMC1869.1, 2008.
- Brown, P. R. A. and Francis, P. N.: Improved measurements of the ice water content in cirrus using a total-water probe, *J. Atmos. Ocean. Tech.*, 12, 410–414, 1995.
- Feldman, R. M. and Valdez-Flores, C.: *Applied Probability and Stochastic Processes*, 2nd Edn., Springer-Verlag, Berlin Heidelberg, 397 pp., doi:10.1007/978-3-642-05158-6, 2010.
- Fujiyoshi, Y., Endoh, T., Yamada, T., Tsuboki, K., Tachibana, Y., and Wakahama, G.: Determination of a *Z-R* relationship for snowfall using a radar and high sensitivity snow gauges, *J. Appl. Meteorol.*, 29, 147–152, 1990.
- Gertzman, H. S. and Atlas, D.: Sampling errors in the measurement of rain and hail parameters, *J. Geophys. Res.*, 82, 4955–4966, 1977.
- Hanesch, M.: Fall velocity and shape of snowflakes, Ph. D. dissertation, Swiss Federal Institute of Technology, Zürich, Switzerland, 117 pp., 1999.
- Heymsfield, A. J., Schmitt, C., Bansemmer, A., and Twohy, C. H.: Improved representation of ice particle masses based on observations in natural clouds, *J. Atmos. Sci.*, 67, 3303–3318, doi:10.1175/2010JAS3507.1, 2010.
- Huang, G.-J., Bringi, V. N., Cifelli, R., Hudak, D., and Petersen, W. A.: A methodology to derive radar reflectivity-liquid equivalent snow rate relations using C-band radar and a 2-D video disdrometer, *J. Atmos. Ocean. Tech.*, 27, 637–651, 2010.
- Hudak, D., Barker, H., Rodriguez, P., and Donovan, D.: The Canadian CloudSat validation project. Proc. Fourth European Conf. on Radar in Hydrology and Meteorology, Barcelona, Spain, 609–612, available at: <http://www.erad2006.org/> (last access: 8 July 2013), 2006.
- Joss, J. and Waldvogel, A.: Raindrop size distribution and sampling size errors, *J. Atmos. Sci.*, 26, 566–569, 1969.
- Kajikawa, M.: Measurement of falling velocity of individual snow crystals, *J. Meteorol. Soc. Jpn.*, 50, 577–584, 1972.
- Korolev, A. and Isaac, G.: Roundness and aspect ratio of particles in ice clouds, *J. Atmos. Sci.*, 60, 1795–1808, 2003.
- Kruger, A. and Krajewski, W. F.: Two-dimensional video disdrometer: a description, *J. Atmos. Ocean. Tech.*, 19, 602–617, 2002.
- Löffler-Mang, M. and Blahak, U.: Estimation of the equivalent radar reflectivity factor from measured snow size spectra, *J. Appl. Meteorol.*, 40, 843–849, 2001.
- Matrosov, S. Y.: A dual-wavelength radar method to measure snowfall rate, *J. Appl. Meteorol.*, 37, 1510–1521, 1998.
- Matrosov, S. Y., Reinking, R. F., and Djalalova, I. V.: Inferring fall attitudes of pristine dendritic crystals from polarimetric radar data, *J. Atmos. Sci.*, 62, 241–250, 2005.
- Matrosov, S. Y., Campbell, C., Kingsmill, D., and Sukovich, E.: Assessing snowfall rates from X-band radar reflectivity measurements, *J. Atmos. Ocean. Tech.*, 26, 2324–2339, doi:10.1175/2009JTECHA1238.1, 2009.
- Mätzler, C.: Microwave dielectric properties of ice, in *Thermal Microwave Radiation: Applications for Remote Sensing*, IET Electromagnetic Wave Series, Vol. 52, edited by: Mätzler, C., Rosenkranz, P. W., Battaglia, A., and Wigernon, J. P., Institute of Engineering and Technology, Stevenage, UK, 2006.
- Mitchell, D. L.: Use of mass- and area-dimensional power laws for determining precipitation particle terminal velocities, *J. Atmos. Sci.*, 53, 1710–1723, 1996.
- Mitchell, D. L. and Heymsfield, A. J.: Refinements in the treatment of ice particle terminal velocities, highlighting aggregates, *J. Atmos. Sci.*, 62, 1637–1644, 2005.
- Mitchell, D. L., Zhang, R., and Pitter, R. L.: Mass-dimension relationships for ice particles and the influence of riming on snowfall rates, *J. Appl. Meteorol.*, 29, 153–163, 1990.
- Nakaya, U. and Terada Jr., T.: Simultaneous observations of the mass, falling velocity and form of individual snow crystals, *J. Fac. Sci., Hokkaido Univ., Ser. 2*, 191–200, 1935.
- Newman, A. J., Kucera, P. A., and Bliven, L. F.: Presenting the snowflake video imager (SVI), *J. Atmos. Ocean. Tech.*, 26, 167–179, 2009.
- Rodgers, C.: *Inverse methods for atmospheric sounding*, World Scientific Publishing, Singapore, 240 pp., 2000.
- Schönhuber, M., Lammer, G., and Randeu, W. L.: One decade of imaging precipitation measurement by 2D-video-distrometer, *Adv. Geosci.*, 10, 85–90, doi:10.5194/adgeo-10-85-2007, 2007.
- Smith, P. L.: Equivalent radar reflectivity factors for snow and ice particles, *J. Climate Appl. Meteorol.*, 23, 1258–1260, 1984.
- Thurai, M. and Bringi, V. N.: Drop axis ratios from a 2-D video disdrometer, *J. Atmos. Sci.*, 22, 966–978, 2005.
- Thurai, M., Hudak, D., and Bringi, V. N.: On the possible use of copolar correlation coefficient for improving the drop size distribution estimates at C band, *J. Atmos. Ocean. Tech.*, 25, 1873–1880, doi:10.1175/2008JTECHA1077.1, 2008.
- Uijlenhoet, R., Porrá, J. M., Torres, D. S., and Creutin, J.-D.: Analytical solutions to sampling effects in drop size distribution measurements during stationary rainfall: Estimation of bulk rainfall variables, *J. Hydrol.*, 328, 65–82, 2006.
- Warren, S. G. and Brandt, R. E.: Optical constants of ice from the ultraviolet to the microwave: A revised compilation, *J. Geophys. Res.*, 113, D14220, doi:10.1029/2007JD009744, 2008.
- York, D., Evenson, N. M., Martinez, M. L., and Delgado, J. D. B.: Unified equations for the slope, intercept, and standard errors of the best straight line, *Am. J. Phys.*, 72, 367–375, 2004.